Computer Methods and Programs in Biomedicine 263 (2025) 108667

Contents lists available at ScienceDirect

Computer Methods and Programs in Biomedicine

journal homepage: https://www.sciencedirect.com/journal/computer-methods-and-programs-in-biomedicine

A computational study of the connection between coronary revascularization and cardio-cerebral hemodynamics

Zhengzheng Yan [a], Dandan Shang [b], Rongliang Chen [a],*, Jia Liu [a], Xiao-Chuan Cai [c]

[a] *Shenzhen Institutes of Advanced Technology, Chinese Academy of Sciences, Shenzhen 518055, PR China*
[b] *Department of Cardiology, Shenzhen Second People's Hospital, the First Affiliated Hospital of Shenzhen University, Shenzhen, 518035, PR China*
[c] *Department of Mathematics, University of Macau, Macao Special Administrative Region of China*

ARTICLE INFO

MSC:
76G25

Keywords:
Computational fluid dynamics
Cardio-cerebral coupling
Coronary artery disease
Parallel computing
Cardiovascular physiology

ABSTRACT

Background and Objective: Some patients experience life-threatening strokes during coronary revascularization. Despite its clinical importance, few numerical studies have investigated the impact of coronary revascularization on cardio-cerebral hemodynamics. This study aims to address this gap by evaluating the effects of eliminating coronary stenosis on both coronary and cerebral blood flow using patient-specific simulations.

Methods: A patient-specific cardio-cerebral arterial network with a 70% stenosis in the left main coronary artery was reconstructed, and computational fluid dynamics were employed to evaluate the effects of eliminating coronary stenosis. The three-dimensional time-dependent incompressible Navier–Stokes equations were discretized using a stabilized P_1-P_1 Galerkin finite element method and an implicit second-order backward differentiation formula. A regional blood flow distribution model, coupled with a lumped Windkessel model, was applied at the outlet boundaries. The 3D pulsatile blood flow was solved using a parallel solver based on a scalable Newton–Krylov–Schwarz algorithm, enabling fast and efficient simulations.

Results: Coronary revascularization significantly improved myocardial blood flow, increasing the coronary fractional flow reserve from 0.742 to 0.904, indicating enhanced myocardial perfusion. However, cerebral hemodynamics were negatively affected, with a 2.49% reduction in blood flow through the main cerebral artery, suggesting an elevated risk of cerebral ischemia. The proposed computational framework demonstrated good parallel scalability across thousands of processor cores.

Conclusions: This study highlights the dual impact of coronary revascularization, improving myocardial perfusion while potentially elevating the risk of cerebral ischemic complications. The efficient computational approach provides a valuable tool for evaluating cardio-cerebral hemodynamics in patient-specific settings, making it suitable for complex and time-intensive simulations.

1. Introduction

Coronary artery disease (CAD) remains the leading cause of mortality worldwide, primarily due to coronary artery stenosis and myocardial ischemia. Coronary revascularization procedures, such as coronary stenting, are commonly employed to enhance the myocardial blood flow and reduce the ischemic risk by modifying vascular anatomy to improve cardiovascular hemodynamics. Over the past decades, these procedures have become a standard treatment for CAD [1]. However, despite their widespread use, coronary revascularization procedures can still result in life-threatening ischemic strokes in some patients, even when significant cerebral artery stenosis is absent [2]. This neurological complication continues to be a major concern, despite significant advancements in revascularization techniques, and remains frequently observed in clinical settings [3,4]. Ischemic stroke occurs when cerebral blood flow is insufficient to meet the metabolic needs of brain tissue, with in-hospital mortality rates reaching as high as 20% [5]. This severe complication highlights the potential negative impact that alterations in coronary artery anatomy, following revascularization, can have on cerebral blood flow. Therefore, it is essential for clinicians to carefully assess patients, particularly those with more than 50% stenosis in carotid artery or large intracranial arteries, prior

---

* Corresponding author.
E-mail addresses: zz.yan@siat.ac.cn (Z. Yan), shangdandan@szseyy.com (D. Shang), rl.chen@siat.ac.cn (R. Chen), jia.liu@siat.ac.cn (J. Liu), cai@colorado.edu (X.-C. Cai).

https://doi.org/10.1016/j.cmpb.2025.108667
Received 23 December 2024; Received in revised form 29 January 2025; Accepted 11 February 2025

to coronary stenting to mitigate the risk of ischemic stroke [6].

Current assessments of stroke risk primarily rely on anatomical stenosis measurements obtained through angiography and other imaging techniques. However, stenosis alone may not always result in functional ischemia, and an incorrect estimation of the ischemic burden could negatively affect graft blood flow [7]. It is therefore crucial to use reliable indicators to assess the hemodynamic significance of arterial stenosis. For coronary blood flow, fractional flow reserve (FFR) is a well-established indicator measured via sensor-equipped guide wires during hyperemia [8–10]. FFR values below 0.75 indicate a need for revascularization. In cerebral circulation, indices such as fractional flow [11] and fractional pressure ratio (FPR) [12,13] have been proposed to assess the functional significance of stenosis. However, there is no universally accepted gold standard equivalent to FFR for evaluating cerebral hemodynamics. Moreover, passing guidewires through the small-diameter vessels of the cerebrovascular system poses higher risks, further complicating the assessment of cerebral blood flow.

In recent years, substantial progress has been made in the application of computational fluid dynamics (CFD) to determine the functional significance of coronary artery disease and ischemic stroke. Notably, non-invasive calculation of FFR from coronary computed tomography angiography (CTA), known as $\mathrm{FFR}_{\mathrm{CT}}$, has shown high diagnostic accuracy for CAD [14,15]. CFD approaches have also been applied to neurology, where they have demonstrated potential for predicting stroke risk. Leng et al. utilized CFD to assess hemodynamic parameters in intracranial atherosclerosis [16,17], and Liu et al. employed CFD to compute FPR, with results comparable to invasive measurements [12]. Rashad et al. applied high-resolution large eddy simulations to investigate complex hemodynamic phenomena in the branching regions that lead to cerebral ischemia in early-stage Moyamoya disease patients, using FLUENT (ANSYS, Inc., USA) with a grid size of approximately 100,000 cells [18]. More recent studies, such as that by Zingaro et al. have integrated CFD simulations with cardiac magnetic resonance to assess stroke risk [19]. These advancements highlight the growing role of CFD in diagnosing and treating cerebrovascular diseases.

Despite these developments, most numerical studies have focused on simulating hemodynamics within a single organ system, such as the coronary [20,21] or cerebral vessels [22,23]. The effect of coronary revascularization on cerebral hemodynamics has not been extensively studied within a three-dimensional, patient-specific cardio-cerebral arterial network, which is of significant clinical relevance. Changes in the geometry of this network can influence the progression of cerebrovascular diseases [24]. The cardio-cerebral network, consisting of the coronary arteries, aortic arch, internal carotid arteries (ICAs), and the circle of Willis (CoW), poses significant computational challenges due to its intricate morphology and complex flow dynamics [25]. Accurate simulation of pulsatile blood flow demands the use of high-resolution meshes to capture the intricate flow characteristics in critical areas such as bifurcations, bends, and stenoses. The nonlinear nature of blood flow, coupled with the substantial computational resources required, further complicates the task of modeling cardio-cerebral hemodynamics. Additionally, patient-specific physiological boundary conditions must be applied at key locations, including the descending aorta, coronary arteries, and cerebral vessels, to accurately reflect real-world hemodynamic conditions. For this reason, a robust computational solver is essential to simulate cardio-cerebral blood flow at high resolutions [26].

In this study, we introduce a regional blood flow distribution model integrated with a 3-element Windkessel lumped parameter model and employ a parallel Newton–Krylov–Schwarz algorithm-based solver to address the computational challenges of simulating 3D patient-specific cardio-cerebral blood flow. This scalable parallel method enables us to investigate the hemodynamic effects of coronary revascularization by artificially removing coronary stenosis and analyzing the resulting hemodynamic changes in both coronary and cerebral circulations. Our results capture the complex fluid dynamics of pulsatile blood flow within intricate arterial geometries, revealing potential cerebral ischemic complications following coronary revascularization. We also evaluate the parallel performance of our solver on a supercomputer, demonstrating its scalability across thousands of processors.

2. Algorithm

2.1. Construction of the patient-specific cardio-cerebral arterial geometry

A 3D patient-specific cardio-cerebral arterial model was reconstructed from high-resolution multi-slice coronary computed tomography angiography (CTA) and magnetic resonance angiography (MRA) scans of a 58-year-old Asian male patient, measuring 172 cm in height and weighting 68 kg. Coronary CTA imaging was performed using a 64-slice scanner (Somatom Definition, Siemens), while MRA imaging was conducted using a 3.0 T magnetic resonance imaging (MRI) system (Magnetom Prisma, Siemens). The coronary CTA images were acquired with a slice thickness of 0.75 mm, a pixel size of 0.326 mm, and an image resolution of 512 × 512 pixels, covering 312 slices. The MRA images had a slice thickness of 0.5 mm, a pixel size of 0.5 mm, and an identical resolution of 512 × 512 pixels, with a total of 488 slices.

Fig. 1 illustrates the reconstructed intricate cardio-cerebral arterial network, including the aortic sinus, aorta, coronary artery, carotid artery, and intracranial/extracranial cerebral arteries. Notable anatomical structures such as the circle of Willis and the aortic arch were also incorporated into the model. Segmentation of arteries with diameters of 1.0 mm or larger was performed using Mimics software (Version 21.0, Materialise NV, Leuven, Belgium). The coronary and cerebral arterial geometries were cropped, merged, and further refined using manual smoothing techniques. An experienced team of medical professionals evaluated the reconstructed model to ensure anatomical accuracy. The final model included 118 outlets, including the descending aorta.

A significant stenosis of approximately 70% was identified in the left main (LM) coronary artery, as depicted in Fig. 1. The stenotic segment measured 11.95 mm in length, with a minimum diameter of 1.7 mm. To simulate the effects of coronary artery revascularization, the stenotic segment was replaced with a normal artery segment, modeling the stent expansion procedure. The baseline diameter of the replacement segment was set at 4.65 mm, based on the distal diameter of the stenosis and clinical stent sizing guidelines. The transition between the stented region and the surrounding healthy arteries was smoothed to ensure geometric continuity.

2.2. Governing equations and boundary conditions

In this study, blood flow in the cardio-cerebral system is modeled as a Newtonian, incompressible fluid with a constant density of $\rho = 1.050\ \mathrm{g/cm^3}$ and viscosity $\mu = 0.035\ \mathrm{cm^2/s}$. The governing equations for the unsteady, incompressible 3D Navier–Stokes equations in the arterial computational domain Ω are expressed as:

$$\frac{\partial \mathbf{u}}{\partial t} + (\mathbf{u} \cdot \nabla)\mathbf{u} = \mu \Delta \mathbf{u} - \frac{1}{\rho}\nabla p \quad \text{in} \quad \Omega \tag{1}$$

$$\nabla \cdot \mathbf{u} = 0 \quad \text{in} \quad \Omega \tag{2}$$

where $\mathbf{u}$ and p represent the blood velocity and pressure, respectively.

A no-slip boundary condition is enforced at the arterial wall Γ_{W}, assuming zero fluid velocity at the wall:

$$\mathbf{u} = \mathbf{0}, \quad \text{on} \quad \Gamma_{\mathrm{W}}. \tag{3}$$

At the inlet boundary Γ_{I}, located at the junction between the left ventricle and the aorta, a time-varying velocity profile is imposed normal to the inlet plane:

$$\mathbf{u} = \mathbf{g} \quad \text{on} \quad \Gamma_{\mathrm{I}},$$

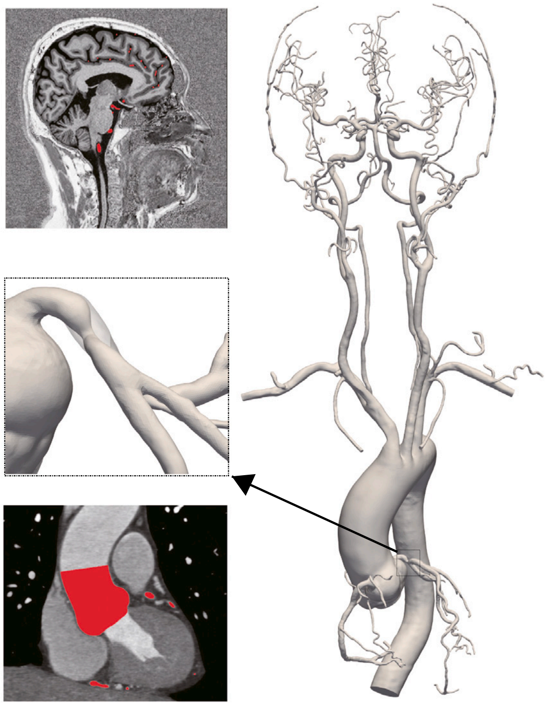

Fig. 1. Reconstructed 3D patient-specific cardio-cerebral vascular model, derived from computed tomography angiography and magnetic resonance angiography images. The model highlights the left main coronary artery stenosis. The stenotic region was replaced with a normal artery segment to simulate the coronary revascularization procedure.

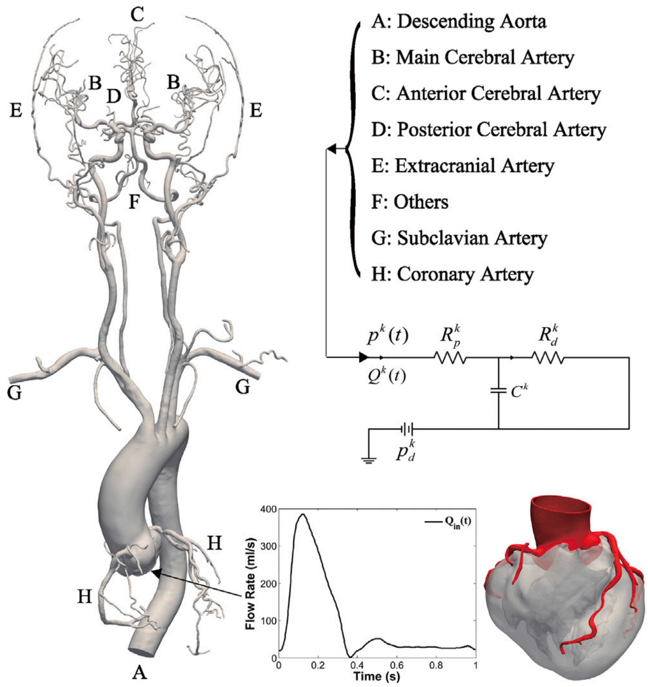

Fig. 2. Boundary condition settings. The time-averaged blood inflow rate is determined based on the reconstructed, subject-specific myocardium. The inflow waveform is adopted from the methodology described by Alastruey et al. [27]. The arterial outlets are categorized into eight distinct groups, with impedance boundary conditions applied to each group accordingly.

Table 1
Grouping of vascular outlets by supplying regions and the corresponding outlet boundary condition parameters.

Group G^i	Vessels	#O	R^i (dyness/cm^5)	C^i (cm^5/dyn)
A	Descending Aorta	1	2164	4.2E−4
B	LMCA, RMCA	27	22 933	4.0E−5
C	LACA, RACA	17	42 167	2.2E−5
D	LPCA, RPCA	6	62 246	1.5E−5
E	LECA, RECA	25	20 424	4.5E−5
F	OTHERS	6	93 370	9.8E−6
G	LSA, RSA	13	8218	1.1E−4
H	CORONARY	23	26 143	3.5E−5

Notes: #O: number of outlets; R^i and C^i: the resistance and peripheral compliance of group G^i; LMCA, RMCA = Left and right main cerebral artery; LACA, RACA = Left and right anterior cerebral artery; LPCA, RPCA = Left and right posterior cerebral artery; LECA, RECA = Left and right extracranial artery; LSA, RSA = Left and right subclavian artery.

where **g** is determined by the time-varying volumetric flow rate Q_{in}. The mean value of Q_{in} over one cardiac cycle corresponds to the cardiac output, which is estimated as $95.2\,\text{cm}^3/\text{s}$ using allometric scaling laws based on the segmented myocardium volume V_{myo} obtained from coronary CTA images. The inflow waveform Q_{in} is derived from phase-contrast magnetic resonance imaging, following the method described by Alastruey et al. [27]. The resulting inflow rate profile is shown in Fig. 2.

An impedance boundary condition was applied at the outlets of the cardio-cerebral arterial network, as described in [28]. The total resistance of the vascular network, R_{T}, was first calculated using the following electrical relation:

$$R_{\text{T}} = \frac{P_{\text{m}}}{\text{CO}}, \tag{4}$$

where $P_{\text{m}} = 93.3\,\text{mmHg}$ represents the mean arterial pressure, determined from the weighted systolic (SBP, 120 mmHg) and diastolic (DBP, 80 mmHg) blood pressures, calculated as $(\text{SBP} + 2\text{DBP})/3$.

Next, the outlets were grouped into eight anatomical regions, as illustrated in Fig. 2. The total resistance and peripheral compliance for each group G^i were defined by:

$$R^i = \frac{R_{\text{T}}}{\text{BFF}^{\text{i}}}, \tag{5}$$

$$C^i = C_{\text{per}} \times \text{BFF}^{\text{i}}, \quad i = 1, \ldots, 8, \tag{6}$$

where BFF^{i} represents the blood flow fraction for group G^i, derived from the total cardiac output. These blood flow fractions were based on literature values from healthy subjects [29,30]. A baseline peripheral compliance value of $C_{\text{per}} = 7.0 \times 10^{-4}\,\text{cm}^5/\text{dyn}$ was used. Within each group G^i, the resistance and capacitance for individual outlet j were computed based on the outlet cross-sectional area A^j, using the following relations:

$$R^j = R^i \frac{\sum (A^j)^{1.5}}{(A^j)^{1.5}}, \tag{7}$$

$$C^j = C^i \frac{\sum A^j}{A^j}, \quad j = 1, \ldots, n, \tag{8}$$

where n is the number of outlets in group G^i. Table 1 summarizes the key parameters for each group, including the number of outlets, resistance, and compliance.

At time t, a time-varying blood pressure $p^k(t)$ is imposed at the kth outlet according to the following equation:

$$\begin{aligned} p^k(t) = {} & [p^k(0) - R_p^k Q^k(0) - p_d^k(0)] e^{-\frac{t}{\tau^k}} + p_d^k(t) \\ & + R_p^k Q^k + \int_0^t \left(\frac{e^{-(t-s)/\tau}}{C^k} \right) Q^k(s) ds, \end{aligned} \tag{9}$$

where $R^k = R_p^k + R_d^k$, $R_d^k = 0.8R^k$, and $\tau^k = R_d^k C^k$. The initial pressure $p^k(0)$ is set to 70 mmHg, while $p_d^k(t)$ represents the downstream pressure, assumed to be zero.

The volume flow rate $Q^k(t)$ through the kth outlet is calculated as:

$$Q^k(t) = \int_{\Gamma^k} \mathbf{u}(t) \cdot \mathbf{n}\, d\boldsymbol{\Gamma}, \tag{10}$$

where $\mathbf{n}$ is the outward unit surface normal at the kth outlet $\varGamma_{\mathrm{O}}^{k}$.

2.3. Discretization

A P_1-P_1 finite element method is employed to discretize the momentum Eq. (1) within the spatial domain. We first define the trial and weighting function spaces as follows:

$$\begin{aligned}
\mathcal{V} &= \left\{ \mathbf{u}(\cdot,t) \;\middle|\; \begin{array}{l} \mathbf{u}(\cdot,t) \in [H^1(\Omega)]^3, \\ \mathbf{u}(\cdot,t) = \mathbf{g} \quad \text{on} \quad \varGamma_{\mathrm{I}} \end{array} \right\}, \\
\mathcal{V}_0 &= \left\{ \mathbf{u}(\cdot,t) \;\middle|\; \begin{array}{l} \mathbf{u}(\cdot,t) \in [H^1(\Omega)]^3, \\ \mathbf{u}(\cdot,t) = \mathbf{0} \quad \text{on} \quad \varGamma_{\mathrm{I}} \cup \varGamma_{\mathrm{W}} \end{array} \right\}, \\
\mathcal{P} &= \left\{ p(\cdot,t) \;\middle|\; p(\cdot,t) \in L^2(\Omega) \right\}.
\end{aligned} \tag{11}$$

The Galerkin weak form of the Navier–Stokes equations is then formulated as: Finding $\mathbf{u} \in \mathcal{V}$ and $p \in \mathcal{P}$ such that:

$$\begin{aligned}
&\rho \int_\Omega \frac{\partial \mathbf{u}}{\partial t} \cdot \boldsymbol{\Phi} d\Omega + \rho\mu \int_\Omega \nabla \mathbf{u} : \nabla \boldsymbol{\Phi} d\Omega + \rho \int_\Omega (\mathbf{u}\cdot\nabla)\mathbf{u} \cdot \boldsymbol{\Phi} d\Omega \\
&\quad - \int_\Omega p \nabla \cdot \boldsymbol{\Phi} d\Omega + \int_\Omega (\nabla \cdot \mathbf{u}) \varphi d\Omega = \int_\Omega \mathbf{f} \cdot \boldsymbol{\Phi} d\Omega,
\end{aligned} \tag{12}$$

for all $\boldsymbol{\Phi} \in \mathcal{V}_0$ and $\varphi \in \mathcal{P}$.

The finite element discretization begins by partitioning the computational domain into an unstructured tetrahedral mesh $\mathcal{T}^h = K$. The finite-dimensional trial and weighting spaces are then defined as:

$$\begin{aligned}
\mathcal{V} &= \left\{ \mathbf{u}(\cdot,t) \;\middle|\; \begin{array}{l} \mathbf{u}(\cdot,t) = \sum_{i=1}^{N_u} \boldsymbol{\Phi}_i^h \mathbf{u}_i^h(\cdot,t), \\ \mathbf{u}(\cdot,t) = \mathbf{g} \quad \text{on} \quad \varGamma_{\mathrm{I}} \end{array} \right\}, \\
\mathcal{V}_0 &= \left\{ \mathbf{u}(\cdot,t) \;\middle|\; \begin{array}{l} \mathbf{u}(\cdot,t) = \sum_{i=1}^{N_u} \boldsymbol{\Phi}_i^h \mathbf{u}_i^h(\cdot,t), \\ \mathbf{u}(\cdot,t) = \mathbf{0} \quad \text{on} \quad \varGamma_{\mathrm{I}} \cup \varGamma_{\mathrm{W}} \end{array} \right\}, \\
\mathcal{P} &= \left\{ p(\cdot,t) \;\middle|\; p(\cdot,t) = \sum_{i=1}^{N_p} \varphi_i^h p_i^h(\cdot,t) \right\},
\end{aligned} \tag{13}$$

where $\mathbf{u}_i^h \in \mathbb{R}^3$ and $p_i^h \in \mathbb{R}$ represent the nodal values of the velocity and pressure functions, respectively, with N_u and N_p denoting the number of nodes for velocity and pressure. Each component of $\boldsymbol{\Phi}_i^h$ and φ_i^h represents a piecewise linear function. To address the failure of the P_1-P_1 element to satisfy the Ladyzenskaja–Babuska–Brezzi (LBB) condition, stabilization terms are introduced. The semi-discrete stabilized finite element formulation of (12) can be expressed as follows: Find $\mathbf{u}^h \in \mathcal{V}^h$ and $p^h \in \mathcal{P}^h$ such that:

$$\begin{aligned}
&\rho \int_\Omega \frac{\partial \mathbf{u}^h}{\partial t} \cdot \boldsymbol{\Phi}^h \, d\Omega + \rho\mu \int_\Omega \nabla \mathbf{u}^h : \nabla \boldsymbol{\Phi}^h \, d\Omega \\
&+ \rho \int_\Omega (\mathbf{u}^h \cdot \nabla)\mathbf{u}^h \cdot \boldsymbol{\Phi}^h \, d\Omega - \int_\Omega p^h \nabla \cdot \boldsymbol{\Phi}^h \, d\Omega \\
&+ \int_\Omega (\nabla \cdot \mathbf{u}^h)\varphi^h \, d\Omega + \underline{\sum_{K\in\mathcal{T}^h} \left(\nabla \cdot \mathbf{u}^h, \tau_c \nabla \cdot \boldsymbol{\Phi}^h\right)_K} \\
&+ \underline{\sum_{K\in\mathcal{T}^h} \left(\frac{\partial \mathbf{u}^h}{\partial t} + (\mathbf{u}^h \cdot \nabla)\mathbf{u}^h + \nabla p^h, \tau_m(\mathbf{u}^h \cdot \nabla \boldsymbol{\Phi}^h + \nabla \varphi^h) \right)_K} \\
&= \int_\Omega \mathbf{f} \cdot \boldsymbol{\Phi}^h \, d\Omega + \underline{\sum_{K\in\mathcal{T}^h} \left(\mathbf{f}, \tau_m(\mathbf{u}^h \cdot \nabla \boldsymbol{\Phi}^h + \nabla \varphi^h)\right)_K},
\end{aligned} \tag{14}$$

where $\boldsymbol{\Phi}^h \in \mathcal{V}_0^h$ and $\varphi^h \in \mathcal{P}^h$. The stabilization terms are underlined, and the parameters τ_c and τ_m are defined as follows:

$$\tau_m = \left(\frac{4}{\Delta t^2} + \left(\mathbf{u}^h \cdot G\mathbf{u}^h\right) + 36 \left(\frac{\mu}{\rho}\right)^2 G : G \right)^{-\frac{1}{2}}, \tag{15}$$

$$\tau_c = \frac{1}{8\tau_m tr(G)}. \tag{16}$$

Here, $G_{ij} = \sum_{k=1}^{3} \frac{\partial \xi_k}{\partial x_i} \frac{\partial \xi_k}{\partial x_j}$ denotes the covariant metric tensor, and $\frac{\partial \xi}{\partial x}$ represents the Jacobian of the mapping between the reference and physical element. The evaluation of $\mathbf{u}$ in τ_m uses the computed solution $\mathbf{u}^h$ at the current timestep.

For temporal discretization, the second-order backward differentiation formula (BDF2) is applied, allowing larger timesteps and reducing overall simulation time. Let $\mathbf{x}^n = (\mathbf{u}^n, p^n)$ denote the velocity and pressure at the nth timestep, and let $S(\mathbf{x}^n)$ represent the semi-discretized system without the time derivative. The BDF2 approximation is given by:

$$\frac{3\mathbf{x}^n - 4\mathbf{x}^{n-1} + \mathbf{x}^{n-2}}{2\Delta t} = S(\mathbf{x}^n), \tag{17}$$

This implicit scheme allows stable and accurate time integration over large timesteps.

2.4. Solver and hardware

After spatial and temporal discretization, at each timestep, the numerical scheme leads to a large, sparse, and nonlinear system as represented in (17), which can be expressed as:

$$\mathbf{F}^n(\mathbf{x}^n) = \mathbf{0}. \tag{18}$$

To efficiently solve this system, we employ a Newton–Krylov–Schwarz (NKS) framework based on domain decomposition methods, combined with an overlapping restricted additive Schwarz (RAS) preconditioner. The NKS approach supports parallel computing, and the RAS preconditioner has been demonstrated to significantly accelerate the convergence of the linear solver. Specifically, an inexact Newton method is applied to solve the nonlinear equations, while the Krylov subspace method, restarted Generalized Minimal Residual (GMRES), is used to compute the search directions within each Newton iteration. The RAS preconditioner enhances the convergence of the GMRES method, thus improving overall computational efficiency.

This solver has proven effective for Navier–Stokes equations in various applications, including airflow [31] and blood flow simulations [32]. The RAS method begins by partitioning the cardio-cerebral arterial computational domain, Ω, into n_p non-overlapping subdomains Ω_i, where $i = 1, 2, \ldots, n_p$, with n_p equal to the number of processors used in parallel simulation. Fig. 3 shows an example of the domain partition into subdomains. For each subdomain Ω_i, overlapping subdomains Ω_i^δ are created by extending δ layers of mesh elements from neighboring subdomains. For each Ω_i^δ, a local Jacobian matrix $\mathbf{J}_i$ is constructed in a manner consistent with the global Jacobian matrix. The restriction operators R_i^δ and R_i^0 are defined to map the degrees of freedom (DOFs) belonging to the overlapping subdomain Ω_i^δ and the non-overlapping subdomain Ω_i, respectively, from the global vector of unknowns. The RAS preconditioner is constructed as the sum of the local preconditioners $\mathbf{B}_i^{-1}$ for each local Jacobian matrix $\mathbf{J}_i$:

$$\mathbf{M}_{\mathrm{RAS}} = \sum_{i=1}^{n_p} (R_i^0)^T \mathbf{B}_i^{-1} R_i^\delta. \tag{19}$$

To efficiently compute the subdomain preconditioner $\mathbf{B}_i^{-1}$, a point-block incomplete LU (ILU) factorization with fill-ins [33] is used instead of the more computationally expensive LU factorization method to balance computational cost with solution accuracy.

By iteratively updating the solution, calculating the step length, solving the Jacobian system using the RAS preconditioned GMRES method, and checking the stopping condition, the algorithm converges to the solution of the nonlinear system (18). The framework of the parallel solver can be summarized as follows:

(a). Initialization: Set $\mathbf{x}_0^n$ as the initial guess, which is usually the solution of the previous timestep $\mathbf{x}^{n-1}$ and set $k = 0$.

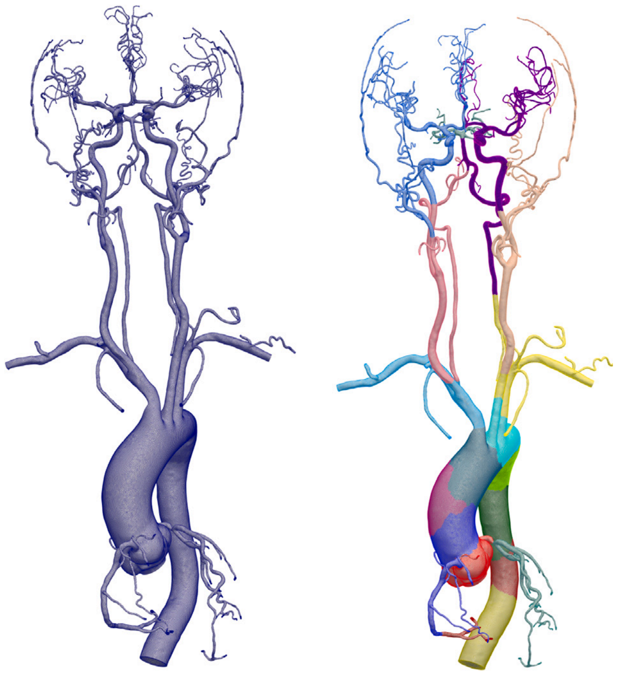

Fig. 3. An example of the cardio-cerebral computational mesh and its partition. Different colors refer different subdomains. Despite their differences in shape and size, the number of elements in each subdomain was made nearly equal to ensure good load balance in parallel computing.

(b). Calculate the function $\mathbf{F}^n(\mathbf{x}_k^n)$ and check the stopping condition: If satisfied, stop and obtain the solution; otherwise, go back to Step (c).

(c). Jacobian system solution: at each Newton iteration, solve the preconditioned Jacobian linear system inexactly using a restarted GMRES method,

$$\mathbf{J}_k^n(\mathbf{M}_k^n)^{-1}\mathbf{y}_k^n = -\mathbf{F}^n(\mathbf{x}_k^n), \tag{20}$$

where $\mathbf{M}_k^n$ is the RAS preconditioner.

(d). Step length calculation and solution update: Use a cubic backtracking line search method to determine the step length λ_k^n and update the solution $\mathbf{x}_{k+1}^n$ in the way:

$$\mathbf{x}_{k+1}^n = \mathbf{x}_k^n + \lambda_k^n \mathbf{s}_k^n, \tag{21}$$

where $\mathbf{s}_k^n = (\mathbf{M}_k^n)^{-1}\mathbf{y}_k^n$ is the search direction calculated in Step (c).

(e). Set $k = k + 1$ and go back to Step (b).

The unstructured tetrahedral computational meshes are generated using ANSYS ICEMCFD (Version 14.5. Canonsburg, PA: ANSYS, Inc.) and partitioned into subdomains using the ParMETIS package [34]. The simulation codes were developed on the top of the open source package PETSc [35], and all the simulations were executed on the TianHe-2A supercomputer at China's National Supercomputing Center at Guangzhou, which is equipped with two 12-core Intel Xeon E5-2692 v2 2.6 GHz CPU processors with 64 GB RAM for each computing node. Visualization of the results was performed using ParaView [36]. The total simulation time is one cardiac cycle $T = 1.0$ s, and the timestep size $\Delta t = 5.0 \times 10^{-3}$ s. The stopping criteria for the NKS algorithm were set as follows: the relative residuals $\zeta \leq 1.0 \times 10^{-4}$ and $\varepsilon \leq 1.0 \times 10^{-6}$ for the linear and nonlinear solvers, respectively. The default overlapping size $\delta = 2$ and levels of ILU fill-ins $\ell = 2$. A maximum restarted iteration $k = 200$ was used for the restart GMRES(k) algorithm.

Table 2
Mesh sets for the mesh independence study.

Mesh	Size	NEs	DoFs
M1	1.92 mm	2.94×10^6	3.89×10^6
M2	0.68 mm	6.69×10^6	5.79×10^6
M3	0.37 mm	1.34×10^7	1.14×10^7
M4	0.23 mm	2.53×10^7	2.01×10^7

Notes: Size: maximum mesh size set on the vascular wall; NE: total number of elements; DoFs: total number of degrees of freedom.

3. Results

This section presents the results from numerical experiments that examine the hemodynamic effects of coronary revascularization on the cardio-cerebral system. We evaluate the mesh independence, pressure variations, ischemia indicators, blood flow distributions, and the solver's parallel performance.

3.1. Mesh independence test

We performed a mesh independence study using four different mesh resolutions, denoted as M1, M2, M3, and M4. The characteristics and details of these meshes are summarized in Table 2 and Fig. 4. Simulations were conducted for each mesh, and pressure profiles were analyzed to determine the convergence of the solution.

Fig. 5 illustrates the comparison of pressure profiles at the aorta and the left anterior descending (LAD) artery across the four mesh resolutions. The results show that mesh M3 provides sufficient accuracy for cardio-cerebral blood flow simulations. Although mesh M4, with a higher node count, yields results comparable to M3, it requires significantly more computational resources. On the other hand, meshes M1 and M2, with fewer nodes, result in less accurate simulations. Therefore, mesh M3 is recommended for future studies as it offers an optimal balance between accuracy and computational efficiency.

3.2. Pressure and ischemia indicators

We then analyzed the hemodynamic status of the cardio-cerebral arterial network before and after revascularization. Fig. 6 displays the pressure field at different phases: systolic, diastolic, and averaged over one cardiac cycle. After revascularization of the left main coronary artery, there is a slight decrease in maximum pressure values in the cardio-cerebral network. Specifically, systolic pressure decreases from 148.4 mmHg to 146.4 mmHg, diastolic pressure decreases from 82.2 mmHg to 81.4 mmHg, and the time-averaged pressure decreases from 106.9 mmHg to 106.0 mmHg. Conversely, minimum pressures show a slight increase after revascularization: from 64.5 mmHg to 64.7 mmHg during systole, from 55.7 mmHg to 55.9 mmHg during diastole, and from 61.1 mmHg to 61.4 mmHg when averaged over time. Notable pressure changes were observed in the LAD and the left circumflex (LCX) arteries, with revascularization reducing the pressure drop caused by stenosis in the LM coronary artery, particularly during the systolic phase and in the time-averaged distribution, resulting in low pressures in the downstream LAD and LCX arteries, which indicated a compromised blood supply.

Fig. 7 further illustrates the time-dependent pressure profiles at various locations, while Fig. 8 provides a comparison of coronary FFR and cerebral FPR. The FFR is calculated as the ratio of the time-averaged pressure at the coronary artery ostium to the pressure downstream of the LM lesion in the LAD artery. Similarly, the FPR is computed as the ratio of the pressure at the right carotid artery to the pressure in the right middle cerebral artery.

A closer examination of Figs. 7 and 8 reveals that, before revascularization, the time-averaged pressures at the aorta and distal ends of the LAD lesion were 106.9 mmHg and 76.8 mmHg, respectively, resulting

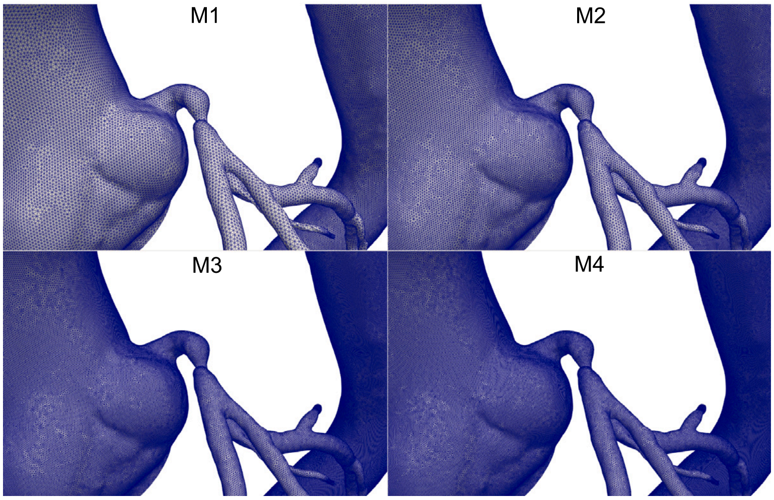

Fig. 4. Mesh comparison near the lesion.

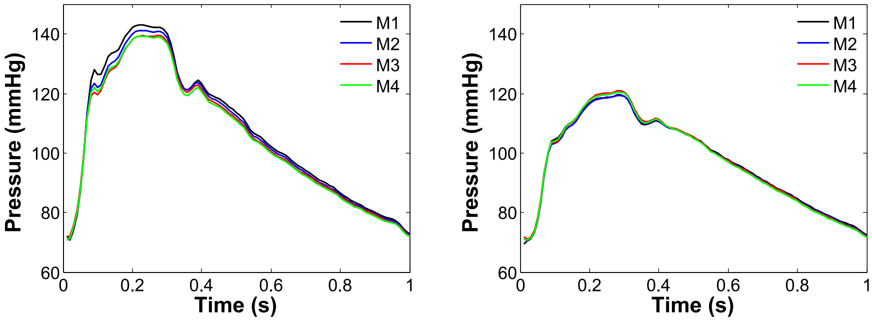

Fig. 5. Pressure profiles at the aorta (left) and the left anterior descending artery (right) obtained by the four meshes, based on the post-revascularization simulations.

in an FFR of 0.742, indicating a high risk of myocardial ischemia and the need for coronary revascularization. After the intervention, the pressure distribution in both the LAD and LCX became more uniform, with the pressure drop reduced to 11.4 mmHg, increasing the FFR to 0.904, confirming the success of the revascularization.

For the cerebral arteries, the pressure distribution before revascularization was relatively smooth, with a pressure drop of 5.91 mmHg between the right carotid artery and the distal right MCA, resulting in an FPR of 0.950. After coronary revascularization, the FPR of the right MCA decreased to 0.940, reflecting a reduction of 0.01 compared to before the revascularization. Since FPR is not the gold standard for cerebral ischemic indicator like FFR for coronary currently, we cannot judge whether the subject had cerebral ischemia, but this reduction in FPR could potentially lead to decreased cerebral perfusion and the occurrence of ischemic stroke.

3.3. Blood flow distribution and manner

Fig. 9 illustrates the flow distribution across various regions of the cardio-cerebral arterial network, allowing for an assessment of the coronary revascularization's impact on both the target arteries and other arterial regions. Coronary revascularization significantly increases flow through the coronary arteries, with the flow rate rising from 2.26 cm^3/s to 4.84 cm^3/s (an increase of 2.58 cm^3/s), and the proportion of total blood flow through the coronary arteries rising from 2.32% to 5.02%. The increased flow in the LAD and LCX arteries demonstrates the procedure's success in improving myocardial perfusion.

Assuming the patient had severe coronary artery disease and two-thirds of the myocardium exhibited perfusion abnormalities prior to revascularization [37], the myocardial blood flow (MBF) increment per unit mass, E_{mbf}, is calculated as:

$$E_{\mathrm{mbf}} = \frac{3\Delta Q_{\mathrm{cor}}}{2\rho V_{\mathrm{myo}}}. \tag{22}$$

where ΔQ_{cor} is the coronary flow increment. This value of $E_{\mathrm{mbf}} = 0.893\,\mathrm{cm}^3/\mathrm{min}/\mathrm{g}$ aligns well with clinical findings, such as those reported by Bober et al. [38], who observed a post-revascularization flow increase of $0.6 \pm 0.7\,\mathrm{cm}^3/\mathrm{min}/\mathrm{g}$ in regions with abnormal perfusion.

While coronary flow increases, the flow in other regions of the network decreases. Notably, flow in the MCA decreases by 2.49%(from 3.533 cm^3/s to 3.445 cm^3/s). The descending aorta experiences the largest decrease, dropping from 65.300 cm^3/s to 62.973 cm^3/s. These reductions warrant further exploration, especially concerning the geometric and physiological factors that may influence this redistribution of blood flow.

3.4. Parallel performance

The performance of the parallel solver was evaluated for strong scalability on mesh M4, which has approximately 20.1 million degrees of freedom (DoFs). Table 3 presents the results for simulations conducted on 480 to 3840 processors. To reduce computational costs, the performance analysis is conducted based on the first 10 timesteps. While the iterations or computation time of the first timestep may have some influence on the results, the strong scalability results show that both the number of nonlinear iterations and GMRES iterations remain consistent or increase gradually as the number of processors increases. This behavior aligns with expectations based on our previous applications of the NKS solver with the RAS preconditioner. These results indicate the scalability of the solver, demonstrating its efficiency in cardio-cerebral blood flow simulations. Note that as we continue to

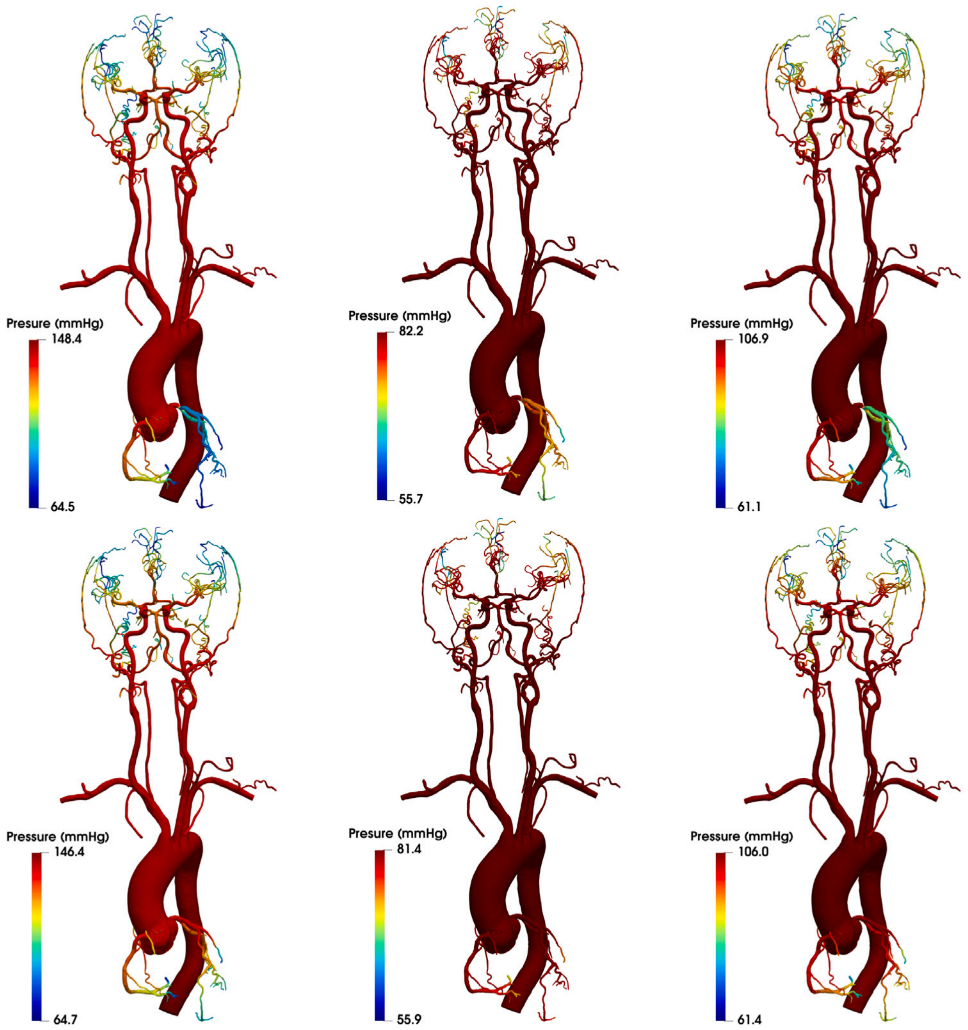

Systolic phase (t=0.23s) Diastolic phase (t=0.85s) Time-Averaged

Fig. 6. Pressure distributions at systole, diastole, and time-averaged values before (top) and after (bottom) coronary revascularization.

Table 3
Parallel performance of NKS algorithm based solver.

n_p	NI	GMRES	Time (s)	Speedup	Ideal	Efficiency
480	3.0	994.57	541.38	1	1	100.00%
960	3.3	1163.67	332.67	1.63	2	81.37%
1920	3.3	1169.73	205.22	2.64	4	65.95%
3840	3.1	923.45	139.85	3.87	8	48.39%

Notes: (n_p) = the numbers of processors;NI = the average number of nonlinear iterations per time step; GMRES = the average number of GMRES iterations per Newton step; Time = the average wall-clock in seconds per time step.

increase the number of processors, the number of GMRES iterations increases rapidly. In this case, two-level methods are required.

4. Discussion

The findings from this study demonstrate the effectiveness of coronary revascularization in improving myocardial perfusion while also highlighting its potential implications for cerebral perfusion under certain conditions. The pressure analysis reveals that revascularization not only reduces the pressure drop across the stenotic coronary artery but also narrows the overall pressure range in the cardio-cerebral vascular network. This narrowing may enhance hemodynamic stability, which is critical for maintaining adequate blood supply to downstream regions. However, the slight decrease in the FPR of the cerebral arteries following the intervention indicates a potential risk to cerebral circulation, necessitating careful monitoring to prevent adverse outcomes, such as ischemic stroke.

The redistribution of blood flow observed post-revascularization underscores the interconnected nature of the cardio-cerebral system. While the coronary arteries benefit significantly from increased flow, there is a reduction in flow to cerebral regions. This phenomenon calls for further investigation to identify the underlying factors, such as geometric variations or physiological adaptations, that contribute to this redistribution.

Furthermore, the strong scalability of the parallel solver employed in this study demonstrates its capability to efficiently handle time-dependent cardio-cerebral simulations. Achieving nearly 50% efficiency on 3840 processors reduces the total wall-clock time for a full cardiac cycle simulation to approximately 7.78 h, enabling faster analysis of complex hemodynamics and accelerating both research efforts and clinical decision-making.

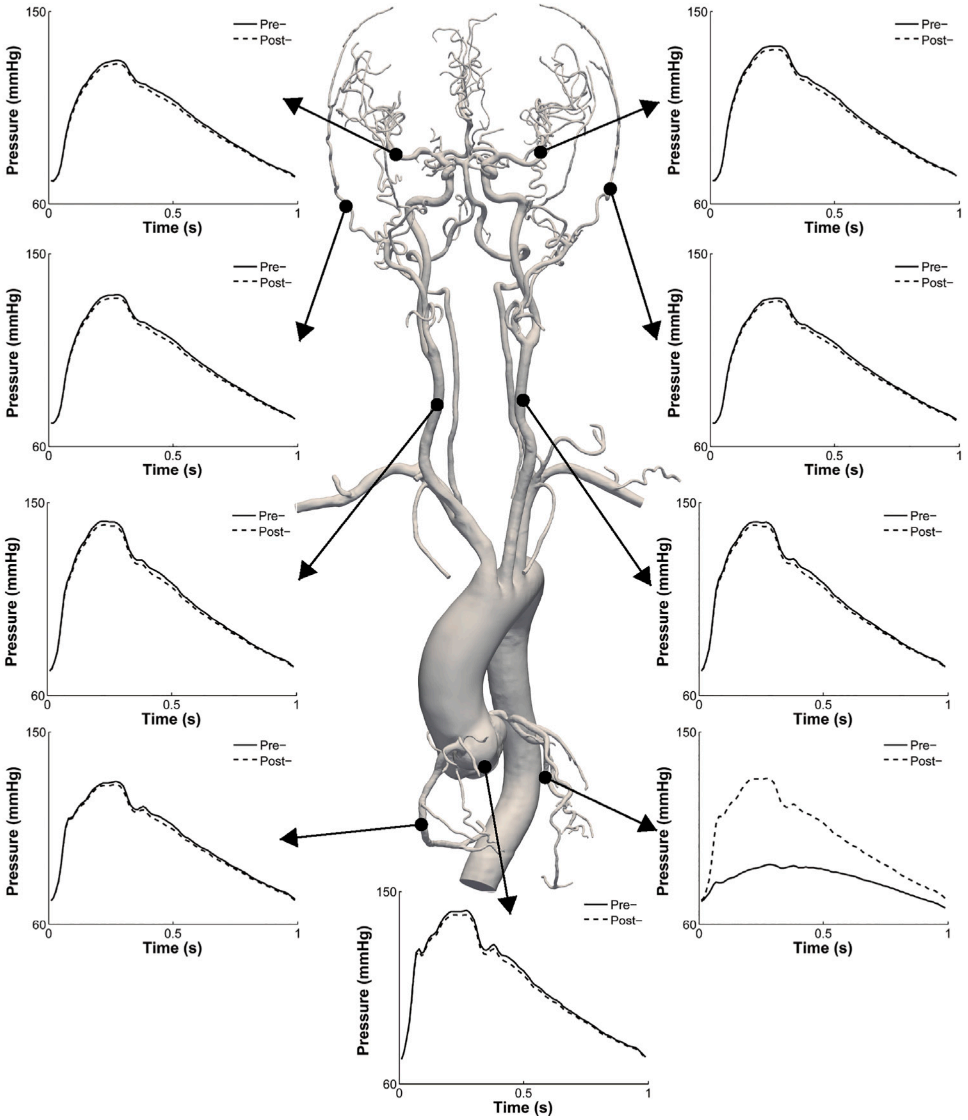

Fig. 7. Pressure throughout the cardio-cerebral arterial network before (solid line) and after (dashed line) revascularization.

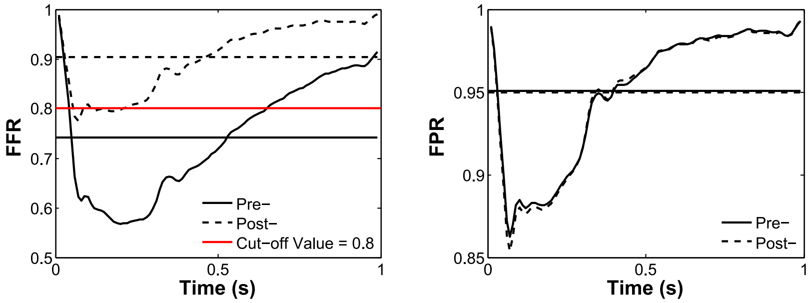

Fig. 8. Fractional flow reserve of the left anterior descending artery (left) and fractional pressure ratio of the left main cerebral artery(right).

5. Limitation

The primary limitation of this study is the exclusion of physiological cerebral blood flow regulation mechanisms, which is a complex and individualized process crucial for maintaining stable cerebral perfusion under varying conditions. Additionally, the lack of clinical validation through invasive measurements, such as direct FPR data, limits the accuracy of the simulation's predictions regarding ischemic stroke risk following coronary revascularization. Invasive FPR measurements are often impractical due to the rapid progression of ischemic stroke and the physiological constraints of the patients. Despite these limitations, the framework established in this study provides a valuable foundation for simulating cardio-cerebral hemodynamics and offers a basis for future research that could incorporate more sophisticated physiological factors and patient-specific modeling.

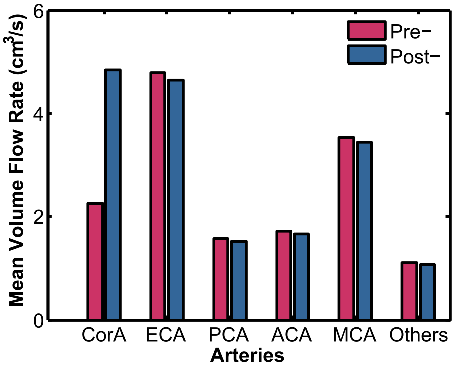

Fig. 9. The mean volume blood flow rate through coronary and cerebral arteries before and after coronary revascularization. CorA = Coronary Artery; ECA = Left and Right Extracranial Artery; PCA = Left and Right Posterior Cerebral Artery; ACA = Left and Right Anterior Cerebral Artery; MCA = Left and Right Main Cerebral Artery.

6. Conclusions

In this study, we developed and implemented a parallel Newton–Krylov–Schwarz algorithm to simulate realistic cardio-cerebral hemodynamic models. The results from our numerical experiments provide critical insights into the impact of coronary revascularization on blood flow dynamics, particularly in mitigating myocardial ischemia while identifying potential reductions in cerebral blood flow, as indicated by the decline in cerebral ischemic indicators. Our findings suggest that revascularization effectively improves coronary blood flow but may slightly reduce cerebral perfusion, thus highlighting the need for careful management of stroke risks in patients undergoing these procedures.

The use of computational fluid dynamics to model the cardio-cerebral system provides a feasible and promising approach for understanding the complex hemodynamic interactions between the heart and brain, particularly in predicting ischemic stroke risks following coronary interventions. Future studies could focus on incorporating more patient-specific models and boundary conditions, as well as physiological regulatory mechanisms, to enhance the accuracy of these simulations and provide deeper insights into the hemodynamics of the cardio-cerebral system. Further improvements in parallel efficiency and algorithm optimization are also essential to make these simulations more clinically applicable.

CRediT authorship contribution statement

Zhengzheng Yan: Writing – original draft, Methodology, Investigation, Funding acquisition, Data curation. **Dandan Shang:** Resources, Data curation. **Rongliang Chen:** Writing – review & editing, Supervision, Methodology, Conceptualization. **Jia Liu:** Funding acquisition, Conceptualization. **Xiao-Chuan Cai:** Writing – review & editing, Supervision, Conceptualization.

Declaration of competing interest

The authors declare that they have no known competing financial interests or personal relationships that could have appeared to influence the work reported in this paper.

Acknowledgments

This work was supported in part by the National Key R&D Program of China (2023YFC2507501), the NSFC (12471413), the Guangdong Basic and Applied Basic Research Foundation (2023A1515012876), the Shenzhen Science and Technology Program (JCYJ20220531100611025), the Key R&D Project of Zhejiang Province (2020C03018), and the Changsha Science and Technology Bureau grant (KH2301001).

References

[1] R.K. Al-Lamee, et al., Revascularization in stable coronary artery disease, BMJ 377 (2022) e067085.
[2] M. Alam, et al., Comparison by meta-analysis of percutaneous coronary intervention versus coronary artery bypass grafting in patients with a mean age of ≥ 70 years, Am. J. Cardiol. 112 (5) (2013) 615–622.
[3] J.K. Devgun, et al., Cerebrovascular events after cardiovascular procedures, J. Am. Coll. Cardiol. 71 (17) (2018) 1910–1920.
[4] K. Yamamoto, et al., Periprocedural stroke after coronary revascularization (from the CREDO-Kyoto PCI/CABG Registry Cohort-3), Am. J. Cardiol. 142 (2021) 35–43.
[5] S.J. Hoffman, et al., Procedural factors associated with percutaneous coronary intervention-related ischemic stroke, JACC: Cardiovasc. Interv. 5 (2) (2012) 200–206.
[6] M.L. Flaherty, et al., Carotid artery stenosis as a cause of stroke, Neuroepidemiology 40 (1) (2013) 36–41.
[7] M. Nagao, et al., Quantification of coronary flow using dynamic angiography with 320-detector row CT and motion coherence image processing: Detection of ischemia for intermediate coronary stenosis, Eur. J. Radiol. 85 (5) (2016) 996–1003.
[8] W.F. Fearon, et al., Fractional flow reserve–guided PCI as compared with coronary bypass surgery, N. Engl. J. Med. 386 (2) (2022) 128–137.
[9] D. Hwang, et al., Prognostic implications of fractional flow reserve after coronary stenting: a systematic review and meta-analysis, JAMA Netw. Open 5 (9) (2022) e2232842.
[10] H. Wang, et al., Simulation of coronary capillary transit time based on full vascular model of the heart, Comput. Methods Programs Biomed. 243 (2024) 107908.
[11] X. Ge, et al., Association of fractional flow on 3D-TOF-MRA with cerebral perfusion in patients with MCA stenosis, Am. J. Neuroradiol. 40 (7) (2019) 1124–1131.
[12] J. Liu, et al., Functional assessment of cerebral artery stenosis: A pilot study based on computational fluid dynamics, J. Cereb. Blood Flow Metab. 37 (7) (2017) 2567–2576.
[13] X. Xu, et al., New evidence for fractional pressure ratio prediction by pulsatility index from transcranial Doppler in patients with symptomatic cerebrovascular stenosis disease, Quant. Imag. Med. Surg. 14 (1) (2024) 264–272.
[14] C.A. Taylor, T.A. Fonte, J.K. Min, Computational fluid dynamics applied to cardiac computed tomography for noninvasive quantification of fractional flow reserve, J. Am. Coll. Cardiol. 61 (22) (2013) 2233–2241.
[15] K.M. Abdelrahman, et al., Coronary computed tomography angiography from clinical uses to emerging technologies, J. Am. Coll. Cardiol. 76 (10) (2020) 1226–1243.
[16] X. Leng, K.S. Wong, D.S. Liebeskind, Evaluating intracranial atherosclerosis rather than intracranial stenosis, Stroke 45 (2) (2014) 645–651.
[17] S. Li, et al., Cerebral hemodynamics and stroke risks in symptomatic intracranial atherosclerotic stenosis with internal versus cortical borderzone infarcts: A computational fluid dynamics study, J. Cereb. Blood Flow Metab. 44 (4) (2024) 516–526.
[18] S. Rashad, et al., The hemodynamic complexities underlying transient ischemic attacks in early-stage Moyamoya disease: an exploratory CFD study, Sci. Rep. 10 (1) (2020) 1–13.
[19] A. Zingaro, et al., A comprehensive stroke risk assessment by combining atrial computational fluid dynamics simulations and functional patient data, Sci. Rep. 14 (1) (2024) 9515.
[20] H.J. Carpenter, et al., On the nonlinear relationship between wall shear stress topology and multi-directionality in coronary atherosclerosis, Comput. Methods Programs Biomed. 231 (2023) 107418.
[21] G. De Nisco, et al., Modelling blood flow in coronary arteries: Newtonian or shear-thinning non-Newtonian rheology? Comput. Methods Programs Biomed. 242 (2023) 107823.
[22] M. Samavaki, et al., Pressure–Poisson equation in numerical simulation of cerebral arterial circulation and its effect on the electrical conductivity of the brain, Comput. Methods Programs Biomed. 242 (2023) 107844.
[23] F. Mezali, et al., Study and modeling of the thrombosis of small cerebral aneurysms, with and without flow diverter, by the lattice Boltzmann method, Comput. Methods Programs Biomed. 233 (2023) 107456.
[24] D. Mukherjee, S.C. Shadden, Inertial particle dynamics in large artery flows–implications for modeling arterial embolisms, J. Biomech. 52 (2017) 155–164.
[25] H. Sun, et al., Numerical study of hemodynamic changes in the Circle of Willis after stenosis of the internal carotid artery, Comput. Methods Programs Biomed. 243 (2024) 107881.
[26] B. Feiger, A. Adebiyi, A. Randles, Multiscale modeling of blood flow to assess neurological complications in patients supported by venoarterial extracorporeal membrane oxygenation, Comput. Biol. Med. 129 (2021) 104155.
[27] J. Alastruey, et al., On the impact of modelling assumptions in multi-scale, subject-specific models of aortic haemodynamics, J. R. Soc. Interface 13 (119) (2016) 20160073.

[28] I. Vignon-Clementel, et al., Outflow boundary conditions for 3D simulations of non-periodic blood flow and pressure fields in deformable arteries, Comput. Methods Biomech. Biomed. Eng. 13 (5) (2010) 625–640.

[29] P.J. Blanco, et al., Blood flow distribution in an anatomically detailed arterial network model: criteria and algorithms, Biomech. Model. Mechanobiol. 13 (6) (2014) 1303–1330.

[30] L. Zarrinkoob, et al., Blood flow distribution in cerebral arteries, J. Cereb. Blood Flow Metab. 35 (4) (2015) 648–654.

[31] Z. Yan, R. Chen, X.-C. Cai, Large eddy simulation of the wind flow in a realistic full-scale urban community with a scalable parallel algorithm, Comput. Phys. Comm. 270 (2022) 108170.

[32] Z. Yan, et al., Impact of pressure wire on fractional flow reserve and hemodynamics of the coronary arteries: A computational and clinical study, IEEE Trans. Biomed. Eng. 70 (5) (2022) 1683–1691.

[33] R. Chen, et al., A parallel non-nested two-level domain decomposition method for simulating blood flows in cerebral artery of stroke patient, Int. J. Numer. Methods Biomed. Eng. 36 (11) (2020) e3392.

[34] G. Karypis, V. Kumar, ParMETIS–Parallel Graph Partitioning and Fill-Reducing Matrix Ordering, Version 4, University of Minnesota, Minneapolis, MN, 2014.

[35] S. Balay, et al., PETSC Users Manual, Tech. Rep. ANL-95/11 - Revision 3.14, Argonne National Laboratory, IL, 2021.

[36] Kitware Inc., ParaView, 2021, https://www.paraview.org.

[37] S. Dorbala, M.F. Di Carli, Cardiac PET perfusion: Prognosis, risk stratification, and clinical management, Semin. Nucl. Med. 44 (5) (2014) 344–357.

[38] R.M. Bober, et al., The impact of revascularization on myocardial blood flow as assessed by positron emission tomography, Eur. J. Nucl. Med. Mol. Imag. 46 (6) (2019) 1226–1239.